



**HAL**  
open science

## Experimental and computational analysis of the mechanical properties of composite auxetic lattice structures

Frédéric Albertini, Justin Dirrenberger, Cyrille Sollogoub, Tobias Maconachie, Martin Leary, Andrey Molotnikov

► **To cite this version:**

Frédéric Albertini, Justin Dirrenberger, Cyrille Sollogoub, Tobias Maconachie, Martin Leary, et al.. Experimental and computational analysis of the mechanical properties of composite auxetic lattice structures. *Additive Manufacturing*, 2021, 47, pp.102351. 10.1016/j.addma.2021.102351. hal-03689590

**HAL Id: hal-03689590**

**<https://hal.science/hal-03689590v1>**

Submitted on 7 Jun 2022

**HAL** is a multi-disciplinary open access archive for the deposit and dissemination of scientific research documents, whether they are published or not. The documents may come from teaching and research institutions in France or abroad, or from public or private research centers.

L'archive ouverte pluridisciplinaire **HAL**, est destinée au dépôt et à la diffusion de documents scientifiques de niveau recherche, publiés ou non, émanant des établissements d'enseignement et de recherche français ou étrangers, des laboratoires publics ou privés.

# Experimental and computational analysis of the mechanical properties of composite auxetic lattice structures

Frédéric Albertini<sup>a</sup>, Justin Dirrenberger<sup>a,\*</sup>, Cyrille Sollogoub<sup>a</sup>, Tobias Maconachie<sup>b</sup>, Martin Leary<sup>b</sup>, Andrey Molotnikov<sup>b,\*</sup>

<sup>a</sup> Laboratoire PIMM, Arts et Métiers Institute of Technology, CNRS, Cnam, HESAM Université, 151 boulevard de l'Hôpital, 75013 Paris, France

<sup>b</sup> RMIT Centre for Additive Manufacturing, RMIT University, 124 La Trobe St, Melbourne VIC 3000, Australia

## Keywords:

Architected materials

Lattice materials

Composite materials

Auxetics

Computational homogenization

Crashworthiness

## ABSTRACT

In this work, the influence of a compliant hyperelastic polymeric phase infiltrated inside stiff auxetic lattices is studied through experimental and numerical approaches. Samples were fabricated using material jetting technology (MJT). The design principle mimics examples of biological materials which combine stiff and compliant materials to attain high superior mechanical properties exceeding the rule of mixtures of both constituent. Two negative Poisson's ratio lattice designs are considered, namely Hexaround and Warmuth cell. Their effective elasto-mechanical properties are investigated through finite element method (FEM) using a homogenization strategy with periodic boundary conditions. A comparison of mechanical properties between lattices and composite lattices, for multiple lattice/matrix volume fractions is discussed and numerical models are validated through a series of compression tests. Results suggest that filling lattices could increase Young's modulus, peak stress, plateau stress and delayed densification of the lattice, hence improving both specific energy absorption (SEA) and absorption efficiency of the considered architected materials. The improvements are attributed to the presence of the matrix acting as a structural support, modifying lattice failure mode from layerwise to shear band breaking. These results expand the design principles for new energy absorption devices based on architected materials.

## 1. Introduction

Architected materials are a rising class of advanced materials that open up new opportunities to populate unoccupied areas of Ashby's materials performance maps [1] and expand their functional properties. The term architected materials encompasses any material obtained through a design process that aims to fulfil a specific set of requirements, in terms of functionality, behaviour, or performance, induced by a particular morphology, *i.e.* the relative topological arrangement between multiple phases, such that some of its materials properties, *e.g.* yield strength/density, are improved in comparison to those of its constituents, due to structure and composite effects [1–4]. Among novel properties associated with a special shape are auxetic materials, which are considered as promising candidate for future engineering applications [5–24].

Auxetics designate a group of architected materials that exhibit negative Poisson's ratio. Such property implies that auxetics expand transversely when stretched, and shrink when compressed, contrary to conventional materials. In the case of three-dimensional isotropic elasticity, Poisson's ratio  $\nu$  is ranging from  $-1$  (unsharable) to  $0.5$

(incompressible, rubber-like). However, most known natural and engineered materials exhibit a positive Poisson's ratio. Studies about auxetic behaviour started in the 80's [5,25,26], drawing increasing attention since then [6–8,10,12–19,27–29]. Reported properties of negative Poisson's ratio materials cover a large spectrum of applications, including acoustic damping [30], improved indentation resistance compared to conventional cellular materials [17,31], improved fracture toughness [32], or as wave-guiding medium [11,33]. Recently, the auxetics have been explored as an energy absorbing medium in order to improve crashworthiness [9,34–36]. While typically metals or composite materials are used to absorb energy either due to plastic deformation [37] or complex failure modes [38], much less attention is given to the morphology of the parts. Often rectangular boxes or axial tubes are utilized due to the ease of manufacturing. However, the use of hybrid or composite materials and selective placement of materials in a part could further enhance the energy absorption capability of these new materials. Ashby and Bréchet [1] defined hybrids as “the combination of two (or more) existing materials so as to allow a superposition of their properties”. This definition encompasses many strategies to produce a

\* Corresponding authors.

*E-mail addresses:* [justin.dirrenberger@ensam.eu](mailto:justin.dirrenberger@ensam.eu) (J. Dirrenberger), [andrey.molotnikov@rmit.edu.au](mailto:andrey.molotnikov@rmit.edu.au) (A. Molotnikov).

hybrid material including combination of architected materials with monolithic ones, referred in this paper as multi-material architected material. Multi-material architected materials aim at combining the benefits from architecture, e.g. lightweight with superior mechanical properties, with those of monolithic materials. It is hypothesized that crashworthiness can be tailored by combining “stiff and compliant” material which is the focus of the present work.

Examples of architected materials that associate stiff and compliant materials can be found in numerous biological materials. The well-studied brick-and-mortar structure of nacre [39–42], exhibit high strength and toughness, far exceeding the properties of its constituents. Another example is turtle shell which consists of the assembly of stiff scales joined by compliant interfaces, providing flexibility under small deformations, but high stiffness under larger deformations [43,44]. Among stiff/compliant engineered architected materials, one can cite stochastic composites, as fibrous composites [45,46] that confer high stiffness for reduced mass, particulate composites [47] increasing stiffness through percolation, or composite metallic foams [48,49] that present increased stiffness, yield stress and dissipated energy compared to simple lattices.

Recently, advances in additive manufacturing technologies (especially resolution and availability to combine multiple materials in the same build) opened up a possibility of manufacturing deterministic composites, such as Interpenetrated Phase Composites (IPC) [50,51] or 2D composite structures [35,52,53] that all report increased stiffness, yield stress and dissipated energy compared to single material structures. Combination of stochastic foams with lattice structures have also been investigated in [54], showing that foam addition stabilizes lattices from buckling, therefore increasing post-buckling strength and exhibiting energy absorption capacity higher than that of both components taken separately.

Fewer studies focused on the combination of hard lattice structures with compliant hyperelastic materials [55,56]. For instance, in the study by Novak et al. [55], auxetic metallic lattices are filled with silicone and it was demonstrated that these composites have a higher elastic modulus and improved compressive strength. However, the study did not investigate the influence of volume fraction and elastic properties of the constitutive phases on the mechanical properties.

Previous studies have also numerically investigated the effect of filling lattices with soft materials and shown its influences on the auxetic properties [57–61]. In other studies, it was reported that it can lead to a delayed buckling of struts and postponement of densification and failure and therefore increasing the elastic modulus and peak stress [53,55,56,62].

In this work, we study the influence of a compliant hyperelastic polymeric phase infiltrated inside stiff auxetic lattices. Specifically, two different auxetic lattices, namely Hexaround [63] and cubic anti-chiral [64] (referred to as Warmuth cell in this work) are designed and manufactured using Polyjet technology. Firstly, we will investigate the effect of elastomeric filling on the elastic behaviour of lattices by the means of computational homogenization. Secondly, finite element simulation based on a finite-strain framework will be performed in order to address the nonlinear mechanical behaviour of auxetic lattices, and compare these results to mechanical tests are performed on additively manufactured samples.

### 1.1. Nomenclature

Throughout this work, the following notation is used:  $x$  for scalars,  $\underline{x}$  for vectors,  $\underline{\underline{x}}$  for 2nd-order tensors,  $\underline{\underline{\underline{x}}}$  for 4th-order tensors,  $\cdot$  for dot product,  $:$  for doubly-contracted dot product,  $\langle x \rangle$  for spatial average, and  $\bar{x}$  for ensemble average.

**Table 1**  
Hexaround cell geometrical parameters for different volume fraction.

$V_f$ (-)	0.05	0.10	0.15	0.20	0.25
$L$ (mm)	6.0	6.0	6.0	6.0	6.0
$a$ (mm)	1.0	1.0	1.0	1.0	1.0
$D$ (mm)	0.39	0.56	0.70	0.83	0.94

**Table 2**  
Warmuth cell geometrical parameters for different volume fraction.

$V_f$ (-)	0.05	0.10	0.15	0.20	0.25
$L$ (mm)	6.0	6.0	6.0	6.0	6.0
$a$ (mm)	1.0	1.0	1.0	1.0	1.0
$D$ (mm)	0.41	0.59	0.73	0.85	0.96

## 2. Experimental procedures

### 2.1. Design of auxetic composite lattice structure

In this work, two types of lattice unit cells are selected due to their ability to show auxetic behaviour, see Figs. 1(a) and 1(b). The Hexaround geometry was proposed by some of the coauthors of the present paper in [63], while the Warmuth cell is a well-known lattice cell with both computational [64] and experimental [65] data available, making it an adequate point of comparison. Unit-cells have been generated using Rhinoceros 3D<sup>1</sup> with the Grasshopper plug-in. The obtained CAD files were exported to STEP and STL files to be used for finite element (FE) modelling and additive manufacturing. Unit-cells are described with respect to geometrical parameters. In the present study, side length of the cubic unit-cells has been chosen equal for both cells, as well as waviness amplitude, for comparison purpose. Only diameter of struts differs, so that each unit-cells could be compared at the same volume fraction  $\rho^*$ , as defined by Eq. (13).

A full description of the Hexaround cell is given in [63]. Struts of the cell are arc-shaped, and negative Poisson ratio (PR) is achieved through inward orientation of arcs. It can be described using 3 parameters:  $L$ , side length of the cubic cell,  $a$ , waviness amplitude, and  $D$ , diameter of the struts (see Fig. 1). The different sets of geometrical parameters result in volume fraction that are displayed in Table 1.

Similarly, the Warmuth cell is generated using the 13th eigen-mode of the regular cubic unit-cell as described in [65] and [66]. The struts are sinusoidal with a circular cross-section. It can be described using 3 parameters:  $L$ , side length of the cubic cell,  $a$ , the amplitude of sine, and  $D$ , diameter of the struts (see Fig. 1b). The different sets of geometrical parameters result in volume fraction that are displayed in Table 2.

Once the lattice structure are defined, their composite counterpart is obtained by filling the voids in the geometry with a soft polymer, see Fig. 1(c).

### 2.2. Materials and methods

Samples have been manufactured using a Stratasys Connex Ob-jet350 printer (multi-material Polyjet material jetting technology). Polyjet technology is based on a liquid droplet deposition method, it can achieve a printing resolution of 600 dpi in both the X- and Y-axes, 1600 dpi in the Z-axis, and a minimum layer thickness of 16  $\mu\text{m}$  [67]. Recent studies have shown its ability to manufacture multi-material composites in a single process [68,69] without porosities between phases. Materials used are VeroWhite (composition: isobornyl acrylate, acrylate monomers, urethane acrylate, epoxy acrylate, acrylate oligomers and photo-initiators) for lattices and TangoBlack+ (urethane acrylate oligomers, Exo-1,7,7-trimethylbicyclo [2.2.1] hept-2-yl acrylate, methacrylate oligomers, polyurethane resin and photo-initiators)

<sup>1</sup> <https://www.mcneel.com>.

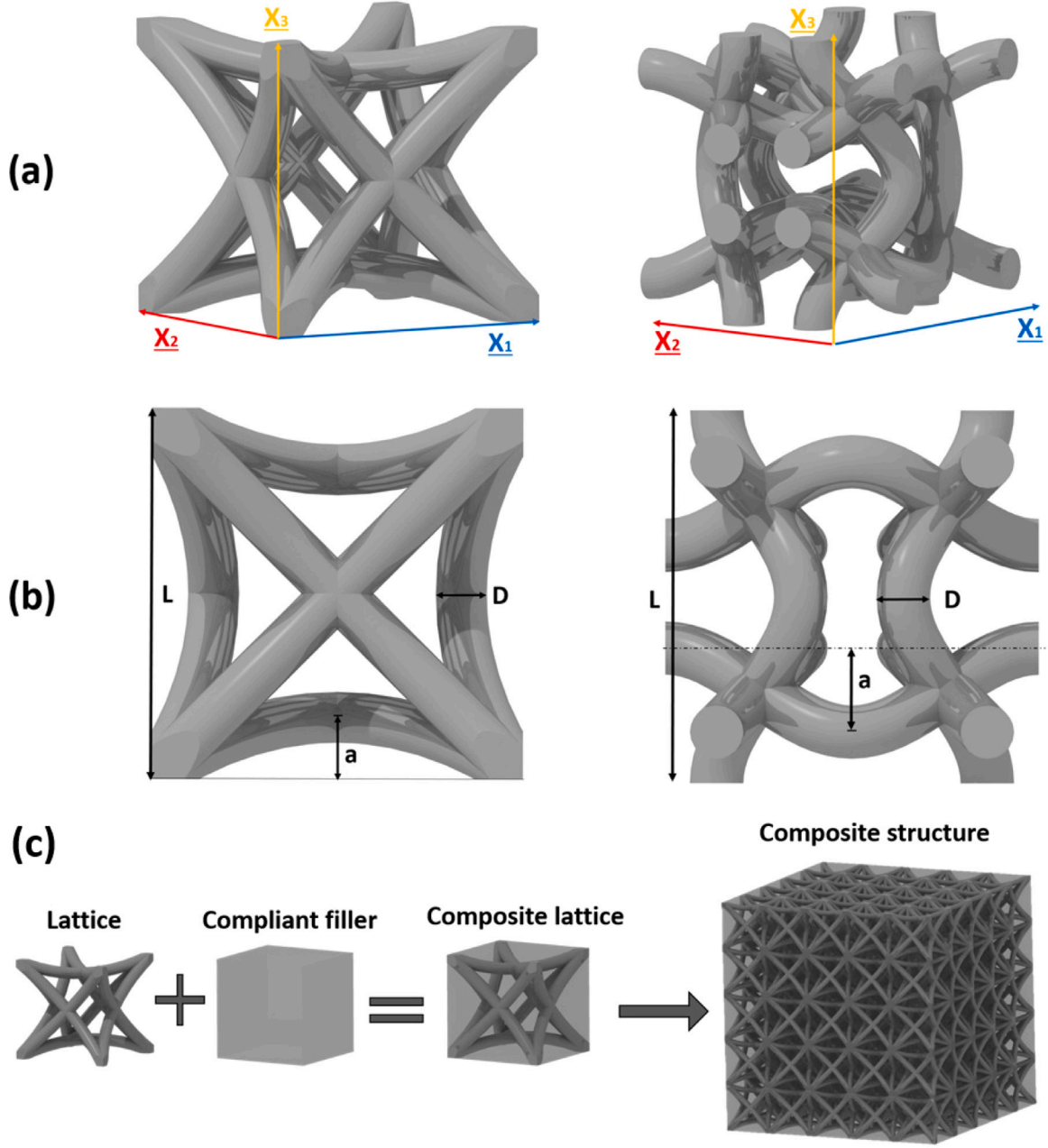


Fig. 1. Hexaround (left) and Warmuth (right) unit-cells, with their periodicity vectors  $X_i$  (a), and geometric descriptions (b), and the strategy to create composite lattice structures (c).

as matrix. Such materials have been used to produce triply periodic minimal surface-based Interpenetrated Phase Composites [50,51] or topological interlocking structures [70]. A full factorial experiment is made, using a total of 16 samples, 4 repetitions of each lattice design and type (Hexaround/Warmuth; lattice/composite lattices). Each sample consists of a cube of 5 unit-cells per side, corresponding to a 30\*30\*30 mm cube, as can be seen on Fig. 2.

VeroWhite is used as constituent for the stiff lattice phase. Its behaviour is considered elasto-plastic, and can be modelled through an isotropic non-linear hardening model [71], given by Eq. (1):

$$R = R_0 + \sum_i^3 Q_i (1 - e^{-b_i p}) \quad (1)$$

Material parameters of VeroWhite's model have been identified from tensile testings (see Fig. 3(a)):  $E = 1.45$  GPa;  $\nu = 0.35$ ;  $\sigma_Y =$

20.0 MPa;  $Q_1 = 19.3$  MPa;  $b_1 = 137.7$ ;  $Q_2 = -39.6$  MPa;  $b_2 = 10.1$ ;  $Q_3 = 51.5$  MPa;  $b_3 = 4.3$ . VeroWhite's density is  $1.175$  g cm $^{-3}$ .

TangoBlack+ is used as the compliant phase. Its behaviour is hyper-elastic and have been modelled using the Arruda-Boyce model [72]. Fitting experimental results from tensile testings, following parameters of A-B model has been identified (see Fig. 3(b)):  $\mu = 0.155$  MPa;  $\lambda = 2.87$  MPa;  $d = 0.30$ . TangoBlack's density is  $1.141$  g cm $^{-3}$ .

A separate study was undertaken to investigate the manufacturability of these composite structures and it was shown that lattices with 20% volume fraction could be manufactured reliably and will be used for the validation of the proposed numerical methods. Due to the nature of Polyjet 3D material jetting process, all lattice samples were filled with support material (a water soluble, wax-like material) that needed to be removed before testing. All lattices were cleaned in an ultrasonic bath with heated solution of caustic soda (5% in concentration), for half an hour, before being rinsed using water jet in order to remove

**Table 3**

Theoretical (CAD) and average measured mass of manufactured samples.

Sample	Mass:	CAD (g)	manufactured (g)
Hexaround (lattice)		6.35	6.75 ( $\pm 0.11$ )
Warmuth (lattice)		6.35	6.68 ( $\pm 0.13$ )
Hexaround (composite lattice)		30.99	31.55 ( $\pm 0.09$ )
Warmuth (composite lattice)		30.99	31.49 ( $\pm 0.10$ )



Fig. 2. Lattice samples of Hexaround and Warmuth structures after manufacturing (left side) shown in red and their composite counterparts filled with TangoBlack+ hyperelastic materials (right side).

the support material. On the other hand, the composite lattices only required a surface cleaning.

Manufactured samples have been weighed to compare with theoretical weights obtained from CAD designs. The measured weights are shown in Table 3. It can be seen that the manufactured lattices and composites are slightly heavier than the theoretically calculated values based on CAD files which is associated with manufacturing spatial accuracy, and minor absorption of moisture from water and environment due to the cleaning process.

### 2.3. Experimental testing

Mechanical behaviour of both manufactured lattice and composite samples has been investigated through compressive tests. An Instron 5969 tensile machine with a 50 kN load cell was used, plates being lubricated in order to reduce friction, using “Super Lube” grease. The applied strain rate was 0.001/s, corresponding to a displacement speed of the plate of 1.8 mm/min. Strain was calculated using recorded plate displacement. Average stress  $\sigma$  have been computed as the applied load  $F$  divided by sample cross section  $S = (5.L).(5.L)$ , with  $S = 900 \text{ mm}^2$  in our case.

### 2.4. Computational homogenization

In this work, computational homogenization is used to predict the effective elastic properties of lattices and composites.

CAD files (STEP format) are meshed using GMSH software [73] with tetrahedral quadratic elements (C3D10). FE analysis has been conducted using Z-Set FE package.<sup>2</sup> A mesh sensitivity study has been performed to ensure numerical accuracy, and is presented in Appendix A.

By computing the volume averaged response under a physical stimulus over a virtual sample that is considered a representative volume element (RVE), one can identify the effective properties of a heterogeneous medium [74–78].

Considering the small deformation hypothesis, constitutive relations are expressed locally in a linear elasticity framework using the generalized Hooke law:

$$\underline{\sigma}(\underline{x}) = \underline{\underline{c}}(\underline{x}) : \underline{\underline{\xi}}(\underline{x}) \quad (2)$$

with  $\underline{\sigma}$  second-order symmetric Cauchy stress tensor,  $\underline{\underline{\xi}}$  second-order symmetric engineering strain tensor, and  $\underline{\underline{c}}$  fourth-order positive definite tensor of elastic moduli. Considering a volume element  $V$ , the macroscopic stress and strain tensors  $\underline{\underline{\Sigma}}$  and  $\underline{\underline{\Xi}}$  are defined by the spatial averages over  $V$  of local stress  $\underline{\sigma}$  and strain  $\underline{\underline{\xi}}$  fields.

$$\underline{\underline{\Sigma}} := \langle \underline{\sigma} \rangle = \frac{1}{V} \int_V \underline{\sigma} dV \quad (3)$$

$$\underline{\underline{\Xi}} := \langle \underline{\underline{\xi}} \rangle = \frac{1}{V} \int_V \underline{\underline{\xi}} dV \quad (4)$$

From Eqs. (2)–(4), it yields the tensor of effective elastic moduli  $\underline{\underline{C}}$ :

$$\underline{\underline{\Sigma}} = \underline{\underline{C}} : \underline{\underline{\Xi}} \quad (5)$$

For periodic boundary conditions, the displacement field  $\underline{u}$  can be dissociated into a part given by the macroscopic strain tensor  $\underline{\underline{\Xi}}$  and a periodic fluctuation field  $\underline{v}$  for any material point  $\underline{x}$  of  $V$ , such that:

$$\underline{u} = \underline{\underline{\Xi}} \cdot \underline{x} + \underline{v} \quad \forall \underline{x} \in V \quad (6)$$

with  $\underline{v}$  the periodic fluctuations vector, *i.e.* taking the same value on two homologous points  $\underline{x}^+$  and  $\underline{x}^-$  of the domain boundary  $\partial V$ . Furthermore, in order to ensure static equilibrium, the traction vector  $\underline{t} = \underline{\sigma} \cdot \underline{n}$  fulfilled antiperiodic conditions, considering  $\underline{n}$  the vector normal to any point  $\underline{x} \in \partial V$  such that,

$$\underline{\sigma}^+ \cdot \underline{n}^+ + \underline{\sigma}^- \cdot \underline{n}^- = \underline{0} \quad (7)$$

$$\underline{v}^+ - \underline{v}^- = \underline{0} \quad (8)$$

The elastic moduli tensor  $\underline{\underline{C}}$  can then be fully identified by applying successively 6 fundamental macroscopic loading, *i.e.* 3 pure extensions, and 3 pure shears. Although not all needed since the Hexaround cell exhibits a cubic symmetry, and the Warmuth cell an orthotropic one, the 6 independent computations are run since the developed methodology is generic and automated. The elastic moduli tensor is identified by applying the macroscopic strain  $\underline{\underline{\Xi}}$ , and measuring the corresponding macroscopic stress components. Using Voigt’s notation, here is an example for cubic elasticity:

$$\begin{bmatrix} \Sigma_{11} \\ \Sigma_{22} \\ \Sigma_{33} \\ \Sigma_{23} \\ \Sigma_{31} \\ \Sigma_{12} \end{bmatrix} = \begin{bmatrix} C_{11} & C_{12} & C_{12} & 0 & 0 & 0 \\ C_{12} & C_{11} & C_{12} & 0 & 0 & 0 \\ C_{12} & C_{12} & C_{11} & 0 & 0 & 0 \\ 0 & 0 & 0 & C_{44} & 0 & 0 \\ 0 & 0 & 0 & 0 & C_{44} & 0 \\ 0 & 0 & 0 & 0 & 0 & C_{44} \end{bmatrix} \begin{bmatrix} E_{11} \\ E_{22} \\ E_{33} \\ 2E_{23} \\ 2E_{31} \\ 2E_{12} \end{bmatrix} \quad (9)$$

Using the identified stiffness tensor, one can compute elastic properties of the cell in every spatial direction. Here, Euler–Bunge [79] angles  $\phi$ ,  $\theta$ , and  $\psi$ , have been used to define 3 orthogonal vectors  $\underline{l}$ ,  $\underline{m}$ , and  $\underline{n}$ , as shown on Fig. 4.

Using the macroscopic stress  $\underline{\underline{\Sigma}}(\phi, \theta, \psi)$  and strain  $\underline{\underline{\Xi}}(\phi, \theta, \psi)$  tensors, effective Young’s modulus  $E(\underline{l})$  and Poisson’s ratio  $\nu^*(\underline{l}, \underline{m})$  are defined as follows:

$$E = \frac{\underline{l} \cdot \underline{\underline{\Sigma}} \cdot \underline{l}}{\underline{l} \cdot \underline{\underline{\Xi}} \cdot \underline{l}} \quad (10)$$

$$\nu^* = -\frac{\underline{m} \cdot \underline{\underline{\Xi}} \cdot \underline{m}}{\underline{l} \cdot \underline{\underline{\Xi}} \cdot \underline{l}} \quad (11)$$

<sup>2</sup> <http://www.zset-software.com>.

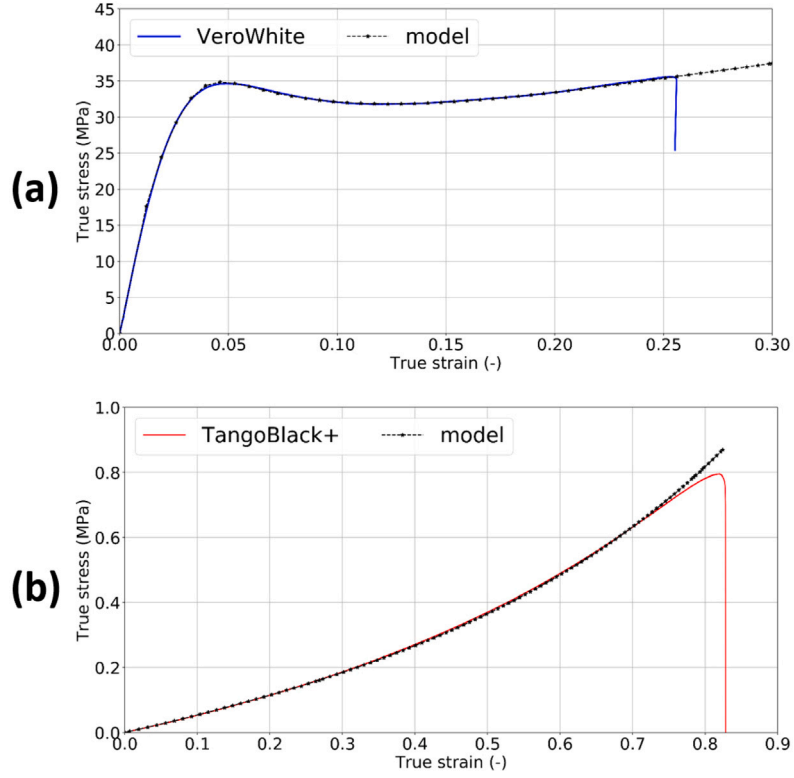


Fig. 3. VeroWhite stress–strain curve and associated model (a); Tango-black+ stress–strain curve and associated model (b).

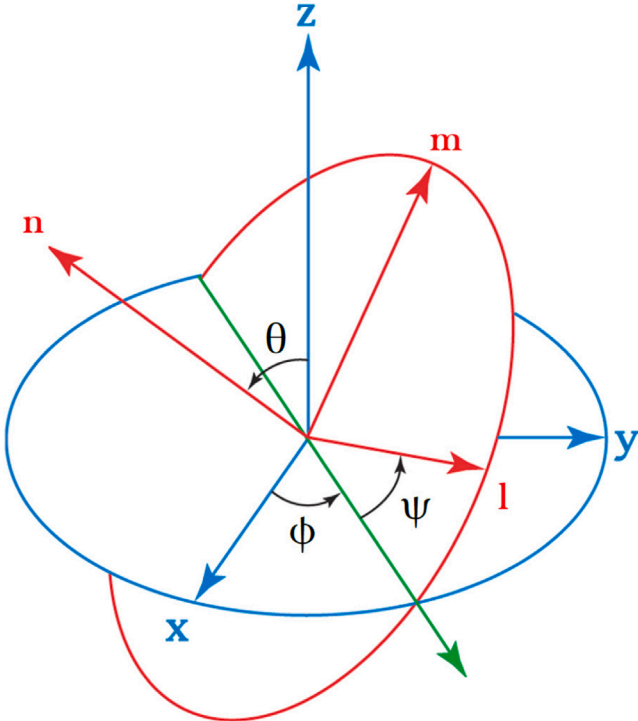


Fig. 4. Euler–Bunge angles.

modulus  $E_0$ , and its volume fraction  $V_f$  :

$$E^* = \frac{1}{E_0 V_f} E \quad (12)$$

volume fraction  $V_f$  being defined as the volume occupied by a periodic cell  $V_{\text{lattice}}$  divided by the cubic volume circumscribed by the cell ( $V_{\text{cubic}} = L^3$ ) as shown on Fig. 5.

$$V_f = \frac{V_{\text{lattice}}}{V_{\text{cubic}}} \quad (13)$$

### 2.5. Computational experiments

In addition to computational homogenization of elastic properties for the lattices, a full-field finite element simulation using nonlinear material models within a finite deformation framework. The objective here is to simulate the compression experiments for comparison. The stress measured is the Boussinesq or 1st Piola–Kirchhoff stress, while the corresponding strain measure is the Green–Lagrange strain. Computations are performed on unit-cells, applying periodic boundary conditions and prescribing macroscopic uniaxial strain component. The choice of working on a periodic unit-cell instead of the full sample geometry is driven by the computational cost of such calculation, which is already very intensive, e.g. 1.2 million degrees of freedom for a composite lattice unit-cell, taking up to 100 h of computation running on a Intel Xeon E5-2640 v4 CPU at 2.4 GHz using 8 cores and 180 GB of RAM. All simulations are performed using tetrahedral quadratic elements (C3D10) and their sizes were determined using mesh convergence analysis, that can be found in Appendix A. The implicit solver MUMPS<sup>3</sup> (MULTifrontal Massively Parallel Solver) is used. Materials behaviour is identified from experimental curves shown in Fig. 3, as presented in Section 2.2. In the context of the present work, no damage was considered in the modelling. This will be the focus a forthcoming paper.

Finally, the normalized modulus of cellular and architected materials can be defined with respect to its constitutive material Young's

<sup>3</sup> <http://mumps.enseeiht.fr/>.

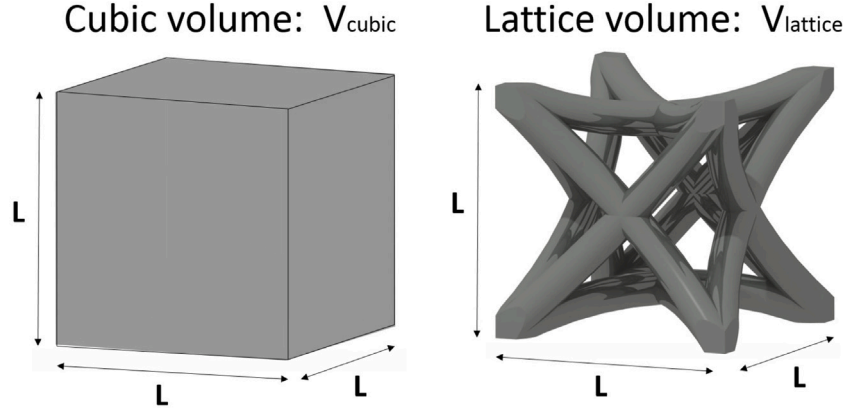


Fig. 5. Representation of  $V_{\text{cubic}}$  and  $V_{\text{lattice}}$ .

Table 4  
Identified Elastic properties of VeroWhite and TangoBlack+.

Material	E (MPa)	$\nu$ (-)
VeroWhite	1450.0	0.35
TangoBlack+	0.65	0.499

### 3. Results and discussions

#### 3.1. Computational homogenization of elastic properties

In this section, a comparison of numerically computed effective elastic properties (normalized Young's modulus  $E^*$  and Poisson's ratio  $\nu$  in this study) with and without compliant matrix is made. Numerical results have been obtained through homogenization for different volume fraction of the presented unit-cells, only varying the diameter of the struts  $D$  to generate five different volume fraction values  $V_f$ : [5, 10, 15, 20, 25%].

In order to compute the elastic properties, the behaviour of both constitutive materials is considered purely elastic isotropic using experimentally identified properties displayed in Table 4.

##### 3.1.1. Normalized modulus

Normalized modulus have been computed for both lattices and composite lattices, plotted in  $(0,0, \psi)$  plan, with regards to the volume fraction of lattices. As both lattices exhibit cubic elastic behaviour – even the Warmuth cell which is not properly cubic from a geometrical viewpoint – only 1/4 of the plane is represented ( $\psi$  is taken between 0 and 90°). A complete 3D map for elastic stiffness of lattices is given in Appendix B. Normalized modulus for both lattice design are displayed in Fig. 6(a) and (c). Normalized volume fractions are obtained by varying the lattice strut diameter, while maintaining waviness amplitude and cell size. The composite lattices normalized modulus is computed considering a rule of mixture for constitutive material  $E_0$ . This corresponds to a theoretical maximum value for composites, hence making it adequate for normalizing the results:

$$E_0 = V_f \cdot E_{VW} + (1 - V_f) \cdot E_{TB+} \quad (14)$$

with  $E_{VW}$  and  $E_{TB+}$ , respectively the Young moduli of VeroWhite and TangoBlack+ phases, as presented in Table 4.

Evolution of Hexaround normalized modulus depending on the loading orientation is presented on Fig. 6(a). It shows that on the plane  $(0,0, \psi)$ , maximum normalized modulus is obtained for  $\psi = 45^\circ$ , for all densities. Maximum normalized modulus for Hexaround lattice is  $E^* = 0.058$  at  $V_f = 5\%$ , and  $E^* = 0.243$  at  $V_f = 25\%$ , respectively. The composite Hexaround lattices show a maximum normalized modulus of  $E^* = 0.167$  at  $V_f = 5\%$ , and  $E^* = 0.250$  at  $V_f = 25\%$ . It is noteworthy that the maximum value of normalized modulus for the Hexaround cell

is not found in the plane  $(0,0, \psi)$  but rather in  $(0, \frac{\pi}{4}, \psi)$ , along  $[111]$  loading orientation as reported in [63].

Evolution of Warmuth normalized modulus depending on the loading orientation is presented on Fig. 6(c). It shows that on the plane  $(0,0, \psi)$ , maximal normalized modulus is obtained for  $\psi = 0^\circ$  (mod 90°) [65] at all volume fractions. Maximal normalized modulus for Warmuth lattice is  $E^* = 0.009$  at  $V_f = 5\%$ , and  $E^* = 0.053$  at  $V_f = 25\%$ . Concerning Warmuth composite lattices, maximal normalized modulus is  $E^* = 0.030$  at  $V_f = 5\%$ , and  $E^* = 0.059$  at  $V_f = 25\%$ .

##### 3.1.2. Influence of filling on normalized modulus

Results show that adding a compliant filling material inside lattices has the obvious effect of stiffening them. However, the stiffening effect seems not only affected by modulus of both phase, but also by the volume fraction distribution between lattice and matrix. It can be seen on Fig. 7(a) and (c) that the filling influence is decreasing with the increase of lattice volume fraction  $V_f$ . At  $V_f = 0.05$ , Hexaround normalized modulus increase by 198%, but at  $V_f = 0.25$  it only increase by 3%. The same trend is observed with Warmuth lattice, suggesting that the modulus ratio between compliant (matrix) and stiff phase (lattice) is critical. Consequence is that filling a lattice may present low influence on its normalized Young's modulus if the lattice is too stiff compared to the filling material, as can be seen for the Hexaround lattice at 25% volume fraction.

##### 3.1.3. Poisson's ratio

Poisson's ratio (PR) of both lattices and composites have been evaluated in plane containing their minimal values, as reported in [63] and [65], i.e. the  $(0,0, \psi)$  plan, for each design regarding lattice volume fraction. As for the modulus, only 1/4 of the plane is represented due to the elastic moduli tensor symmetry. PR of both lattice designs are displayed in Fig. 6(b) and (d).

Evolution of Hexaround PR depending on the loading orientation is presented on Fig. 6(b). It shows that on the plane  $(0,0, \psi)$ , minimal PR is reached for  $\psi = 45^\circ$  for all volume fractions. Minimal PR for Hexaround lattice is  $\nu^* = -0.60$  at  $V_f = 5\%$ , and  $\nu^* = -0.01$  at  $V_f = 25\%$ . Concerning Hexaround composite lattices, minimal PR is  $\nu^* = -0.01$  at  $V_f = 5\%$ , and  $\nu^* = 0.04$  at  $V_f = 25\%$ . As can be seen on Fig. 7(b), incorporating a soft phase into a rigid lattice structure shows a non-monotonic influence over Hexaround PR, but it's influence is decreasing with the increase of lattice volume fraction  $V_f$ .

Evolution of Warmuth PR depending on the loading orientation is presented on Fig. 6(d). It shows that on the plane  $(0,0, \psi)$ , minimal PR is found for  $\psi = 0^\circ$  (mod 90°) at all volume fractions. Minimal PR for Warmuth lattice is  $\nu^* = -0.35$  at  $V_f = 5\%$ , and  $\nu^* = -0.32$  at  $V_f = 25\%$ . Concerning Warmuth composite lattices, minimal PR is  $\nu^* = 0.44$  at  $V_f = 5\%$ , and  $\nu^* = -0.20$  at  $V_f = 25\%$ . In contrast to Hexaround structure incorporation of a soft phase into the Warmuth lattice structure strongly increases Warmuth PR at low volume fraction, but it's influence is decreasing while lattice volume fraction  $V_f$  increases.

### 3.1.4. Influence of filling on Poisson's ratio

One can observe on Fig. 7(b) and (d) that filling increases Poisson's ratio value, making it closer to TangoBlack+ and thus reducing auxeticity of the lattices. It can be explained by the presence of the elastomer that hinders the deformation of the lattice. However, the influence of the filling is non-monotonic. A strong influence of lattice volume fraction can be observed: the higher the lattice volume fraction, the lesser the effect of filling on Poisson's ratio.

## 3.2. Compression tests

Results of compression tests are presented on Fig. 10, displaying lattice, composite lattices and pure TangoBlack+ stress/strain curves. Compression plates were lubricated in order to minimize friction in both simple lattice and composite lattice during the compression tests. In order to make a relevant comparison, TB+ curve is a FE compression simulation of a TB+ cube of same dimensions as experimental composite samples are compared. TB+ behaviour used for simulations was identified from experimental testings, shown in Fig. 3. The complete experimental records are displayed in Appendix C. These results are compared with those from the corresponding computational experiment.

### 3.2.1. Hexaround cell

Hexaround lattices present a layerwise failure, each bump corresponding to the collapse of one floor. The average peak stress is 0.83 MPa, average densification occurs at 47% strain. The average measured Young's modulus is 22.15 MPa. Hexaround composite lattices compression test begins with a linear part with an average measured Young's modulus of 31.04 MPa, followed by plastic deformation and failure of the lattice due to the formation of shear band. An average peak stress of 2.63 MPa is reached, then densification occurs at 65% strain. It can be seen on Fig. 8 that the composite lattice displays very different behaviour and instead of layerwise failure a shear band formation and failure is observed. This difference can be explained by the presence of the matrix that prevents the lattice to collapse layerwise, delaying deformation of the struts and distributing stress more evenly as shown by FE simulations in Fig. 9. Average peak stress is increased from 0.83 to 2.63 MPa (a 217% increase), and densification is delayed from an average 47% to 65% strain. Measured Young's modulus is increased by 40%.

### 3.2.2. Warmuth cell

Warmuth lattice compression behaviour starts with a linear elastic part, followed by a plateau. Damage occurs resulting in stress peaks until densification. An average peak stress of 0.58 MPa is reached and densification occurs around 49% strain. From the linear elastic part, the average measured Young's modulus is 3.75 MPa. Composite lattices compression behaviour begins with a small linear part until 2.5% strain, followed by non-linear elasticity. Plateau, damage and densification followed. An average peak stress of 2.83 MPa is reached, then densification occurs at an approximate 61% strain. Average measured Young's modulus is 19.05 MPa. For this design, peak stress is increased from 0.58 to 2.83 MPa (a 388% increase), and densification is delayed from 49% to 61% strain. Average measured Young's modulus is increased by 400%.

The influence of filling with a compliant phase on the Warmuth lattice mechanical properties has a more important effect compared to that of Hexaround composite lattice structure. This observation can be explained by the fact that Warmuth lattice properties are lower than the Hexaround, being 5.9 times more compliant. Therefore it can be concluded that the lower the lattice base modulus, the greatest the increase of mechanical properties due to filling strategy. Table 5 provides a comparison of mechanical properties for all samples. Simulation is yielding an overestimation of the mechanical response for the lattices, due to defect-free nature of the computational samples, contrary to

the actual experimental samples that were obtained through additive manufacturing. The small discrepancies between computational experiments and computational homogenization regarding the value of  $E$  is due to the nonlinear nature of the matrix phase, which is not taken into account properly in the computational homogenization scheme, due to the linear hypothesis.

## 3.3. Crashworthiness evaluation

The crashworthiness properties of lattices and composite lattices are compared using the Specific Energy Absorption (SEA). This experimental measure is considered a reliable indicator to compare the Energy Absorption (EA) with regard to the weight of the samples. EA is calculated as the area under stress-strain curves, yielding a mechanical work density, depending on the uniaxial strain  $\xi$  and principal stress measure  $\sigma$  in the following manner:

$$EA(\xi) = \int_0^{\xi} \sigma(\xi) d\xi \quad (15)$$

SEA is defined as the sum of the energy density dissipated and elastic energy density stored in the sample volume until densification, divided by the mass of the sample,  $m$ . Densification happens when cell struts reach contact with one another, and is achieved when peak stress value is reached a second time. Thus, SEA is expressed in  $J g^{-1} cm^{-3}$ , and can be calculated such that:

$$SEA = \frac{1}{m} \int_0^{\xi_d} \sigma(\xi) d\xi \quad (16)$$

VeroWhite and TangoBlack+ having very close density (respectively  $1.175 g cm^{-3}$  and  $1.141 g cm^{-3}$ ), and the lattice volume fraction being  $V_f = 20\%$ , one can infer that composite lattices are approximately 5 times heavier than lattices samples. Thus in order to dissipate more energy than the lattice, composite lattices must at least dissipate 5 times more energy.

Another pertinent criterion is the absorption efficiency  $\eta$ , expressed in Eq. (17). It may be used to compare the efficiency of lattices and composite lattices, with regards to idealized absorber in the case of a total uniaxial strain  $\xi$  of 100%.

$$\eta = \frac{\int_0^{\xi_d} \sigma(\xi) d\xi}{\sigma_{peak} \cdot l} \quad (17)$$

Both energy criteria have been plotted on Fig. 11, with Hexaround SEA and absorption efficiency on the left, and Warmuth ones on the right.

### 3.3.1. Hexaround cell

Despite the fact that composite Hexaround lattices exhibit higher stiffness and yield stress than simple ones, it can be seen in Fig. 11 that lattices SEA is higher before densification happens. This can be explained by the fact that lattices samples are 5 times lighter than their composite counterparts. Average lattices SEA at densification is  $1.00 J g^{-1} cm^{-3}$ . However, as the filling material is delaying densification, Hexaround composite lattices SEA at densification is finally 22% higher than simple ones, reaching  $1.22 J g^{-1} cm^{-3}$ . Concerning absorption efficiency, Hexaround lattices reach an average 30.27% and composite lattices attain 52.73%. The increase efficiency can be explained by the delayed densification as well as the change of deformation behaviour: layerwise failure being less efficient than a plateau-like plasticity in this case.

### 3.3.2. Warmuth cell

In the case of the Warmuth cell, SEA of composite lattices are always higher than their simple lattice counterparts, being 60% higher at densification (see Fig. 11). Warmuth lattices reach an average SEA of  $0.77 J g^{-1} cm^{-3}$ , and composite lattices an average  $1.23 J g^{-1} cm^{-3}$ . Increased modulus and yield stress and especially delayed densification

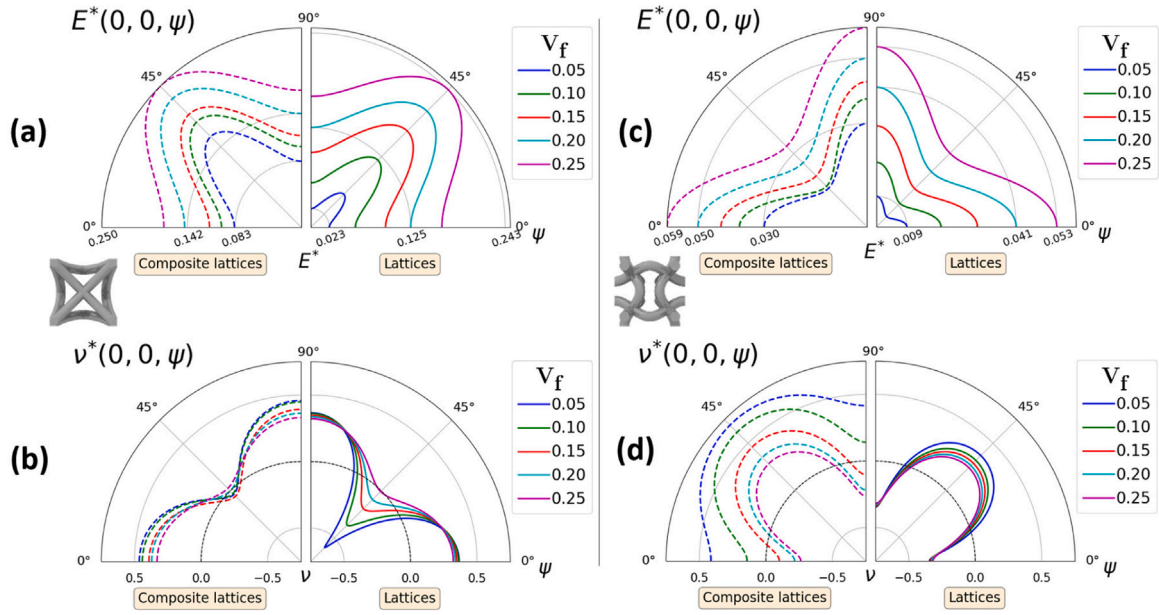


Fig. 6. Hexaround (left) and Warmuth (right) elastic properties depending on loading orientation and lattice volume fraction.

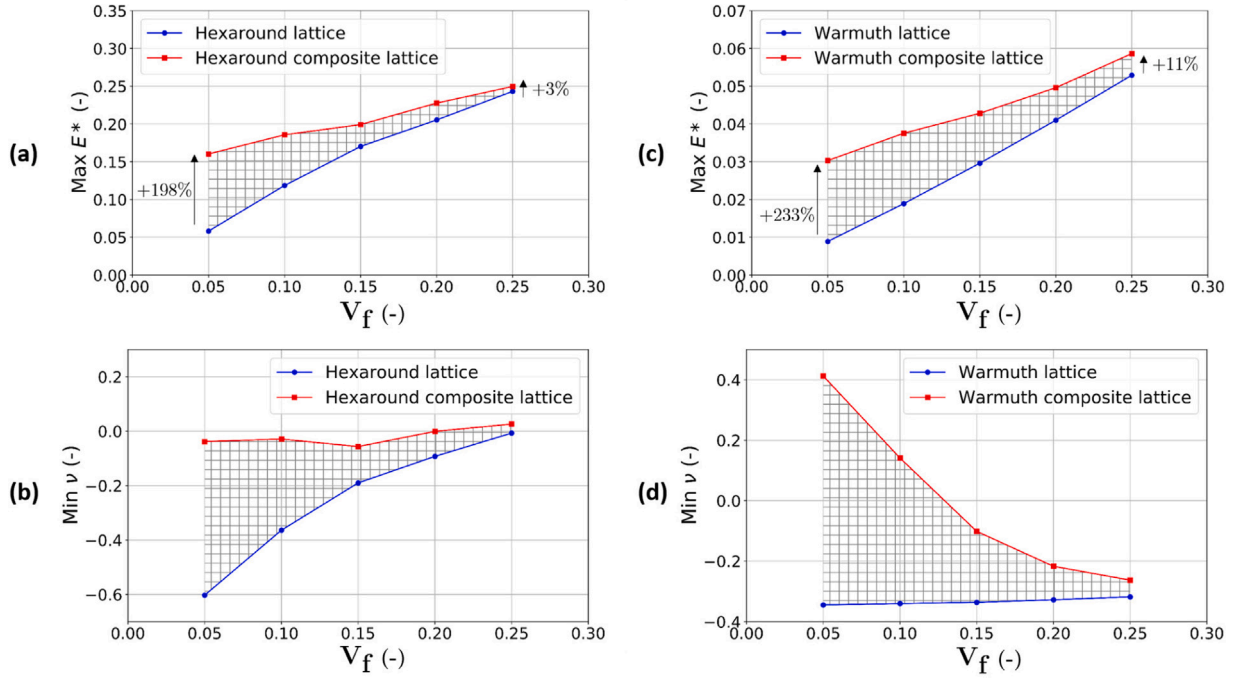


Fig. 7. Influence of the filling soft phase on maximum normalized modulus (a)(c) and minimal Poisson's ratio (b)(d), for different lattice volume fraction.

**Table 5**  
Comparison between lattices and composite lattices properties.

Sample	$\bar{E}_{exp}$ (MPa)	$E_{hom}$ (MPa)	$E_{simul}$ (MPa)	$\bar{\xi}_d$ (-)	$\bar{\sigma}_{peak}$ (MPa)
Hexaround (lattice)	22.15 ( $\pm 1.3$ )	36.04	36.01	0.47 ( $\pm 0.04$ )	0.83 ( $\pm 0.05$ )
Hexaround (composite)	31.04 ( $\pm 0.9$ )	42.24	39.13	0.65 ( $\pm 0.04$ )	2.63 ( $\pm 0.09$ )
Warmuth (lattice)	3.75 ( $\pm 0.3$ )	11.08	10.96	0.49 ( $\pm 0.05$ )	0.58 ( $\pm 0.05$ )
Warmuth (composite)	19.05 ( $\pm 1.1$ )	20.75	20.72	0.61 ( $\pm 0.07$ )	2.83 ( $\pm 0.10$ )

are responsible for increased SEA. The absorption efficiency of Warmuth lattices reaches an average 33.09% and composite lattices attain 48.31%. The increase efficiency occurs due to the delayed densification.

Crashworthiness properties of both lattices and composite lattices are reported in Table 6. One can conclude that filling auxetic lattices

with compliant material increases SEA at densification, but has a less pronounced effect for intermediate strains. Specifically, the observed increase in SEA is linked to the ability of the composite lattices to delay densification. A consequent increase in absorption efficiency is observed for both unit-cells, stemming from different mechanisms : the

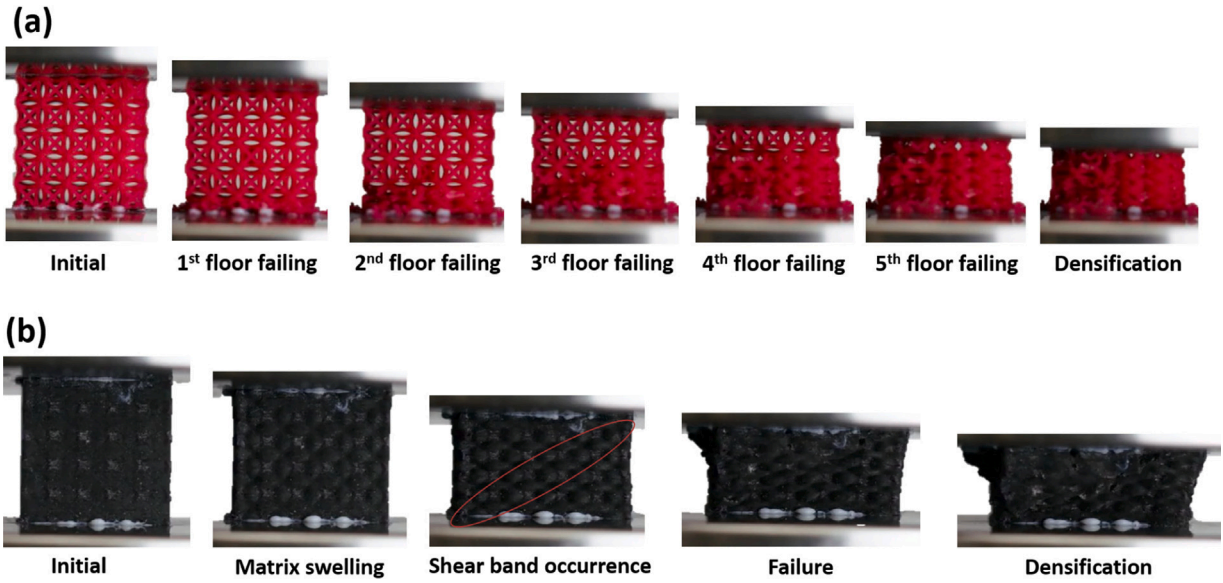


Fig. 8. Change in the mode of failure from layerwise for the hexaround lattice (a) to shear band for the composite hexaround lattice (b).

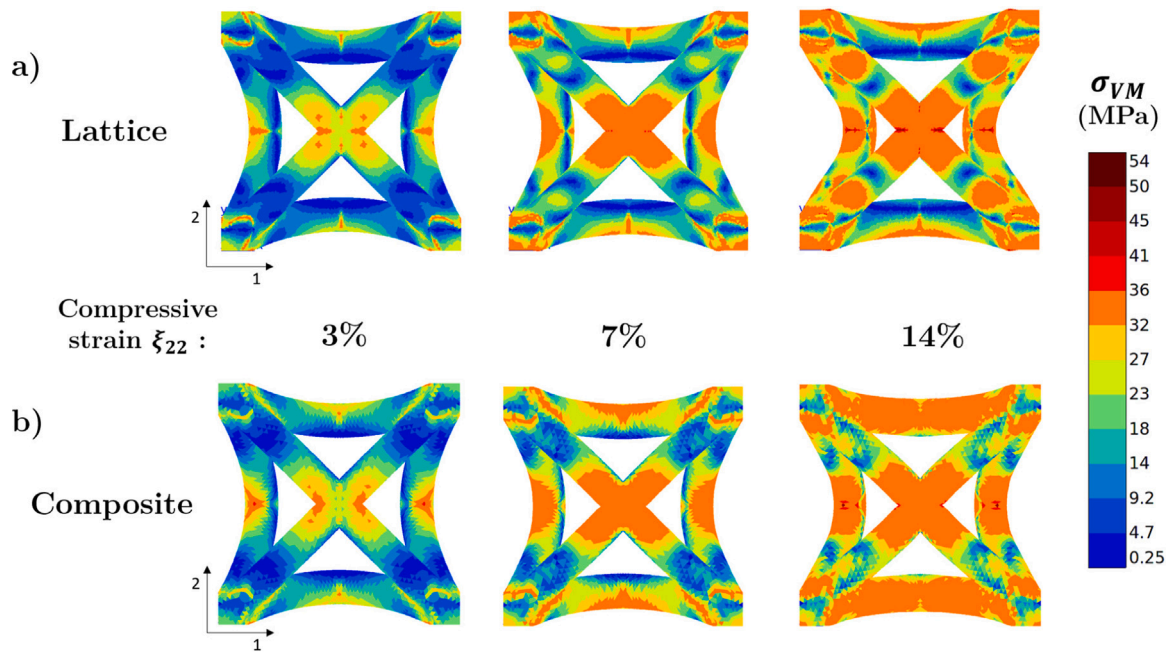


Fig. 9. Von Mises equivalent stress maps within the truss for both simple (a) and composite (b) lattices at 3 levels of uniaxial compressive strain, resulting from FE simulations.

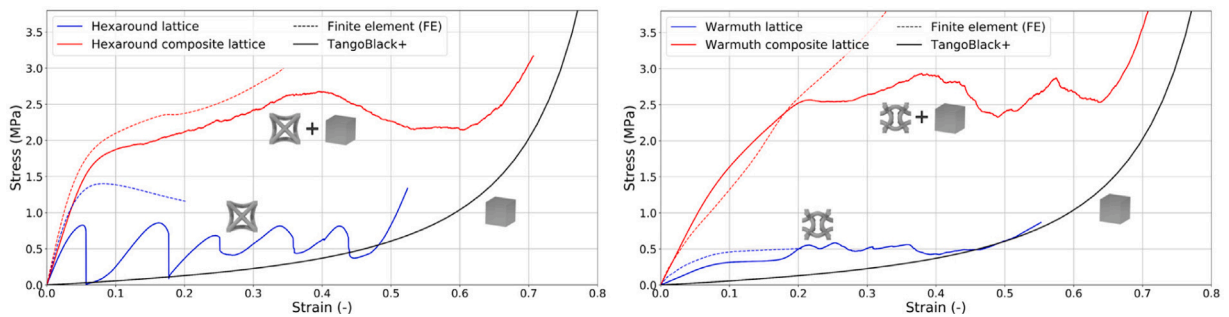


Fig. 10. Strain/stress plot, Hexaround (left) and Warmuth (right).

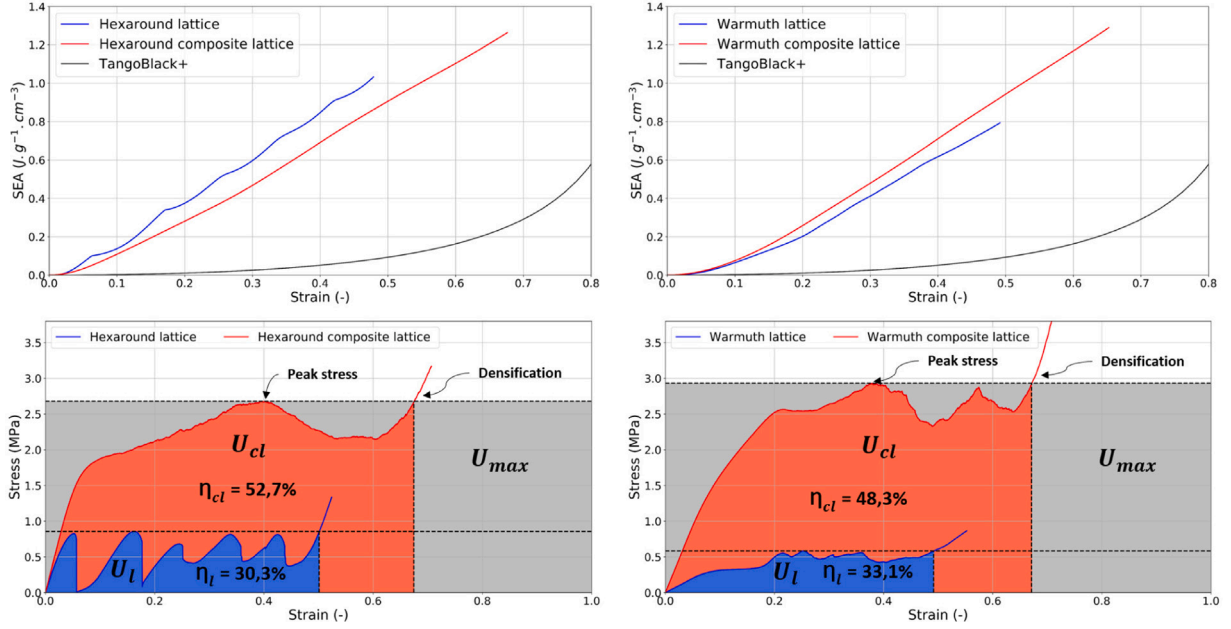


Fig. 11. SEA and Efficiency plot, Hexaround (left) and Warmuth (right).

Table 6

Experimentally recorded crashworthiness properties.

Sample	SEA $\xi = \xi_d$ (J.g <sup>-1</sup> .cm <sup>-3</sup> )	$\eta$ (%)
Hexaround (lattice)	1.00 ( $\pm$ 0.05)	30.27 ( $\pm$ 2.1)
Hexaround (composite)	1.22 ( $\pm$ 0.09)	52.73 ( $\pm$ 2.5)
Warmuth (lattice)	0.77 ( $\pm$ 0.07)	33.09 ( $\pm$ 1.5)
Warmuth (composite)	1.23 ( $\pm$ 0.11)	48.31 ( $\pm$ 5.2)

Hexaround lattice is subjected to a different deformation behaviour from filling and both lattices benefit from delayed densification.

#### 4. Discussion

In this work, we studied the effect of filling a compliant material into two auxetic structures. It was shown that composite lattices exhibit increased stiffness compared to their monolithic counterparts and the increase of the stiffness was varied depending on the lattice volume fraction. This observation is consistent with results reported in [55] and [56]. However, in [56] the elastic modulus tends to increase from filling with high volume fraction lattices, even with high lattice volume fraction, which is in contradiction to our results. This can be explained by the high stiffness of the elastomers used, being 3300 to 6000 times

stiffer than TB+, therefore providing a more efficient support. On the other hand, when the lattice structure is infiltrated with a harder polymer than used for the struts, a decreased or no change in specific Young's modulus has been reported in [62] and [80]. Evolution of composite lattices Young's modulus seems to be very dependent on the base material constitutive properties, specifically the modulus ratio between lattice and matrix  $E_{\text{lattice}}/E_{\text{matrix}}$ .

When considering the Poisson's ratio our results indicate different trends to some earlier published work. For instance, Hexaround lattice minimal PR increases with volume fraction, until being completely non auxetic at high volume fraction. This trend is also followed by the composite Hexaround lattice structure where low volume fraction composite lattices show less auxeticity than simple lattices. Warmuth lattice minimal PR is less sensitive to the volume fraction evolution, but the maximal PR is higher for low volume fraction lattices. Composite Warmuth lattices exhibit lowest PR at high lattice volume fraction, where the matrix is having less influence on its behaviour. The presence of the soft phase tends to oppose auxetic deformation behaviour, making composite lattices less auxetic than simple ones. Increased PR from filling is also observed in [35,53] and [56], but no investigation on the effect of lattice volume fraction was made. In [61], composite auxetics exhibit a similar trend to Hexaround lattice where matrix increases the

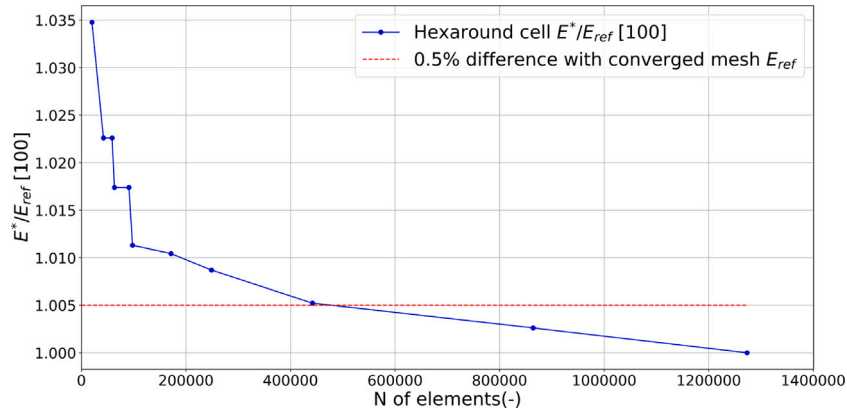


Fig. A.12. Mesh sensitivity study for the Hexaround cell.  $E_{\text{ref}}$  being the converged normalized Young's modulus.

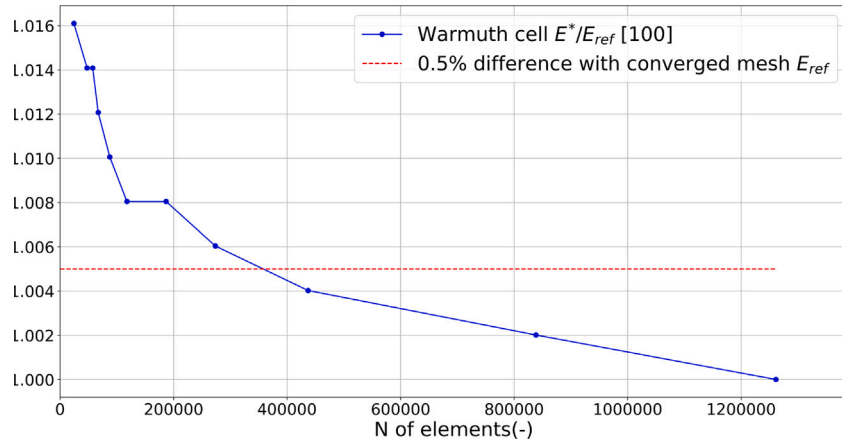


Fig. A.13. Mesh sensitivity study for the Warmuth cell.  $E_{ref}$  being the converged normalized Young's modulus.

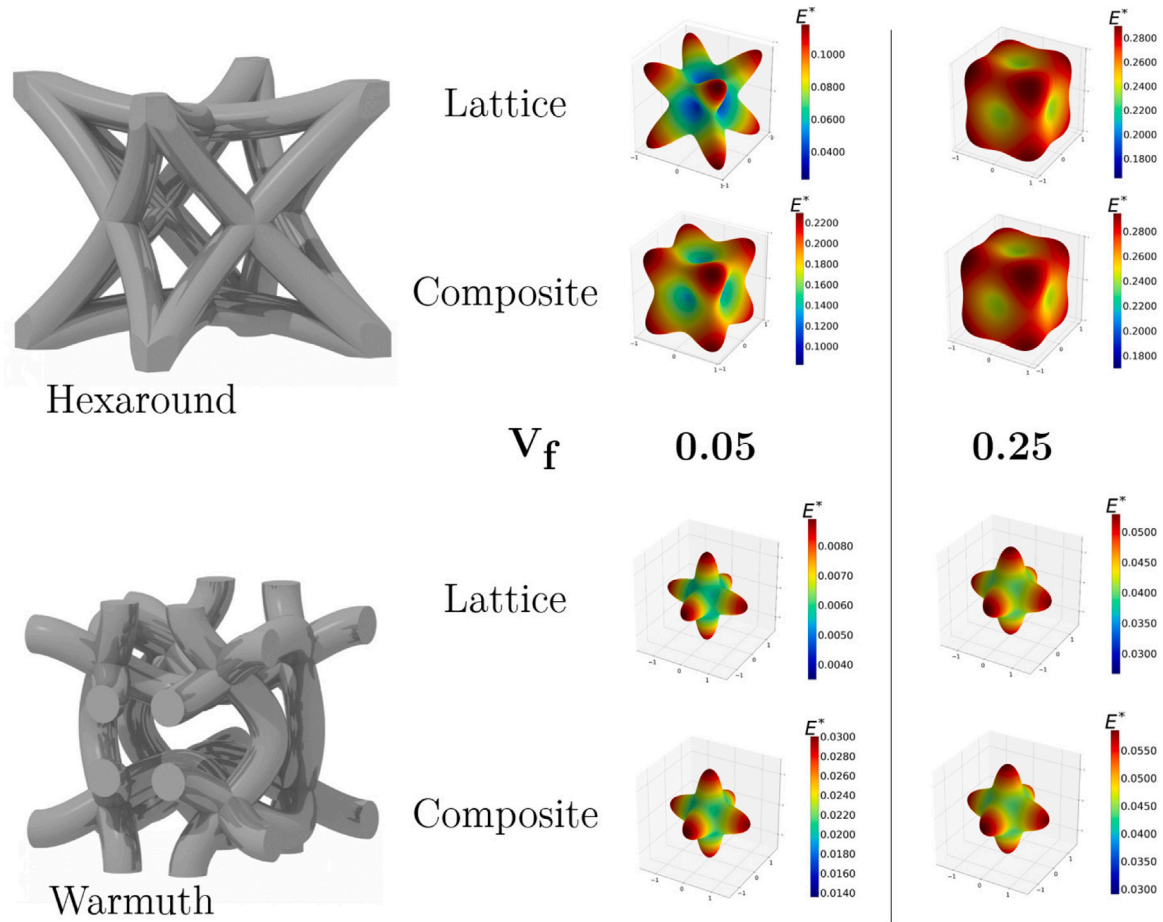


Fig. B.14. 3D representation of the normalized directional elastic stiffness (Young's modulus as a function of orientation) for Hexaround and Warmuth cells at 0.05 and 0.25 volume fraction for both truss and composite lattices.

composite PR at low lattice volume fraction but its influence is decreasing with higher lattice volume fraction. As well as for normalized Young's modulus, effective Poisson's ratio of composite lattice depends on modulus ratio  $E_{lattice}/E_{matrix}$ , as observed by [60]. While the present study only considered one pair of materials, further experiments could shed more light on the effect of different material properties ratio on the elastic properties of the composite lattice structures.

The compression tests revealed an important increase of stress level as well as peak stress resulting from filling with a soft phase. It showed that the composite stress level was not following a rule of mixture

but demonstrated superior properties compared to its constituents. The stress resulting from the interaction between structure and matrix should be taken into account, as explained in [62]. Furthermore, it was observed that densification of lattices is postponed when filled with an elastomeric polymer. The opposite phenomenon has been observed on lattices filled with hard epoxy, in [62] and [80]. The delay in the densification was linked to a significant improvement in SEA and AE. In order to reveal mechanisms behind changes in deformation behaviour from filling further in-situ mechanical test using X-ray imaging should be conducted.

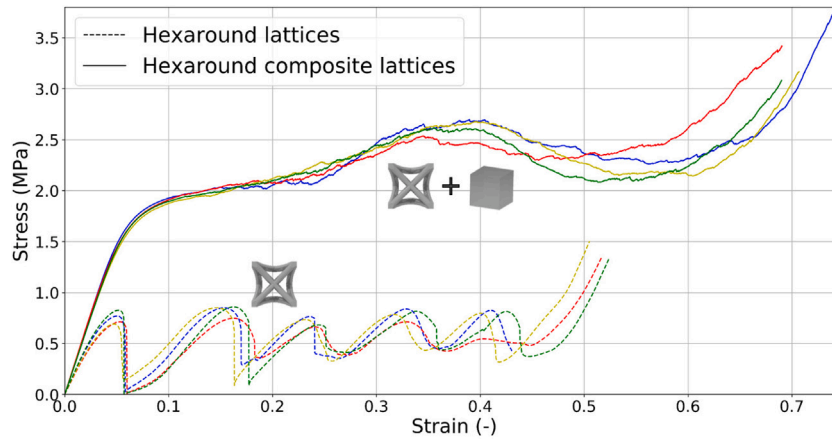


Fig. C.15. Stress/strain plot, Hexaround lattices and composite lattices compression test.

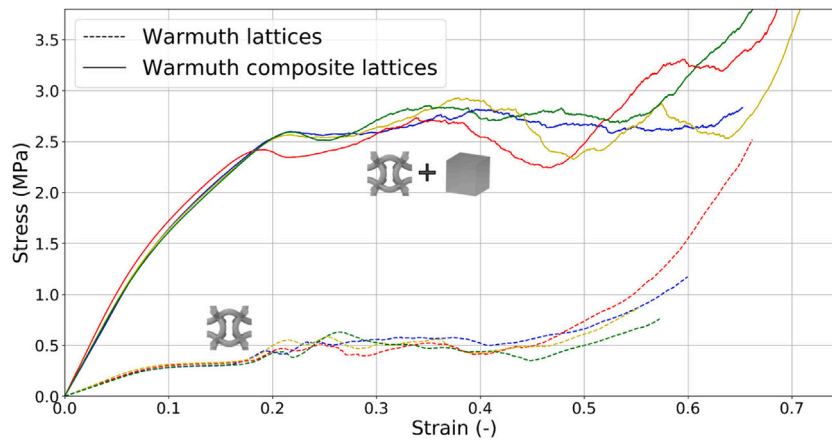


Fig. C.16. Stress/strain plot, Warmuth lattices and composite lattices compression test.

## 5. Conclusions and perspectives

In this work, mechanical properties of 2 different auxetic lattices filled with hyperelastic polymer are studied through both numerical and experimental approaches. Following conclusion can be drawn from this work:

1. Effective elastic properties ( $E^*$  and  $\nu$ ) of lattices and composites are compared using the numerical homogenization method, based on periodic boundary conditions. Five relative densities  $V_f$  of both Hexaround and Warmuth cell, obtained by varying struts diameter  $D$ , are compared. Results showed an increase of normalized Young's modulus due to filling, dependently on lattice initial modulus: the Hexaround see low change of modulus at high volume fraction, but important increase at low volume fraction. Warmuth cell being more compliant, its stiffness is highly increased at all lattice volume fraction. TangoBlack+ being nearly incompressible with a Poisson ratio close to 0.5, composite lattices Poisson's ratio is increased compared to simple lattices, with a strong influence of lattice volume fraction. Therefore, the lower the volume fraction of the lattice structure the larger the increase in its stiffness.
2. Lattices and composite lattices samples have been manufactured using Connex350 with VeroWhite and TangoBlack+ materials. Lattices were both manufactured at 20% volume fraction  $V_f$ . Compression tests have been performed, showing that filling lattices with soft material induces an increase of Young's modulus (up to +316% for Warmuth cell, and +40% for Hexaround one), yield stress and peak stress, and delayed densification.

Finite element analysis shows good agreement with composite lattices experiments in the linear elastic part, but deviated in the plasticity region since the material behaviour did not account for damage. Good agreement between experiments and computational homogenization validated the selected strategy over full-field analysis.

3. During compression tests, the Hexaround lattice exhibits a layer-wise failure mode, that is represented on stress/strain curves by five "bumps", corresponding to the five floors breaking one after the other. Hexaround composite lattices exhibit a completely different failure, involving shear band breaking. Warmuth lattice also shows a progressive failure, floor crumbling one after the other, but it cannot be clearly observed on stress/stress curves. Warmuth composite lattice exhibits structural buckling before a shear band breaking.
4. Comparison of Specific Energy Absorption and Absorption Efficiency  $\eta$  is carried between manufactured lattices and composite lattices. The Warmuth composite cell exhibits superior SEA at all strain, up to  $1.23 \text{ J g}^{-1} \text{ cm}^{-3}$  at densification, compared to simple lattice, which is not the case of the Hexaround that only displays superior SEA thanks to delayed densification, up to  $1.22 \text{ J g}^{-1} \text{ cm}^{-3}$ . Both cells benefit of an increased absorption efficiency from filling, mainly because of delayed densification.

### CRedit authorship contribution statement

**Frédéric Albertini:** Investigation, Methodology, Software, Writing – original draft. **Justin Dirrenberger:** Conceptualization, Supervision,

Methodology, Writing – review & editing. **Cyrille Sollogoub**: Supervision, Methodology, Writing – review & editing. **Tobias Maconachie**: Investigation, Writing – review & editing. **Martin Leary**: Writing – review & editing, Supervision. **Andrey Molotnikov**: Conceptualization, Supervision, Methodology, Writing – review & editing.

#### Declaration of competing interest

No author associated with this paper has disclosed any potential or pertinent conflicts which may be perceived to have impending conflict with this work. For full disclosure statements refer to <https://doi.org/10.1016/j.addma.2021.102351>.

#### Acknowledgements

F. Albertini and J. Dirrenberger acknowledge funding by the France–Australia Science Innovation Collaboration program as well as funding from Académie Française. Financial support from the French Department of Higher Education, Research and Innovation is gratefully acknowledged for funding F. Albertini's PhD scholarship. J. Dirrenberger acknowledge partial funding from the Agence Nationale de la Recherche, France through the ANR JCJC SCOLASTIC project (grant no. 16-CE08-0009). A. Molotnikov would like to acknowledge the financial support from the Rod Rickards Fellowship from the Australian Academy of Science.

#### Appendix A. Mesh convergence analysis

To ensure a mesh-independent response, a mesh convergence analysis has been performed, as shown in [Figs. A.12 and A.13](#). Here, the number of elements in a mesh is considered sufficient if an error lower than 0.5% compared to a converged mesh is computed, the [100] relative elastic modulus being the object of the comparison.

#### Appendix B. Elastic stiffness maps for lattices

See [Fig. B.14](#).

#### Appendix C. Complete experimental curves

See [Figs. C.15 and C.16](#).

#### References

- [1] M.F. Ashby, Y. Bréchet, Designing hybrid materials, *Acta Mater.* 51 (2003) 5801–5821.
- [2] O. Bouaziz, Y. Bréchet, J.D. Embury, Heterogeneous and architected materials: A possible strategy for design of structural materials, *Adv. Energy Mater.* 10 (1–2) (2008) 24–36, <http://dx.doi.org/10.1002/adem.200700289>.
- [3] Y. Bréchet, J.D. Embury, Architected materials: Expanding materials space, *Scr. Mater.* 68 (1) (2013) 1–3.
- [4] Dirrenberger J., Towards an integrated approach for the development of architected materials, 2018, URL <https://hal.sorbonne-universite.fr/tel-02047005>.
- [5] R.S. Lakes, Foam structures with a negative Poisson's ratio, *Science* 235 (1987) 1038–1040.
- [6] R.S. Lakes, Deformation mechanisms in negative Poisson's ratio materials: structural aspects, *J. Mater. Sci.* 26 (1991) 2287–2292.
- [7] G.W. Milton, Composite materials with Poisson's ratios close to -1, *J. Mech. Phys. Solids* 40 (5) (1992) 1105–1137.
- [8] D. Prall, R.S. Lakes, Properties of a chiral honeycomb with a Poisson's ratio of -1, *Int. J. Mech. Sci.* 39 (3) (1997) 305–314.
- [9] F. Scarpa, J.R. Yates, L.G. Ciffo, S. Patsias, Dynamic crushing of auxetic open-cell polyurethane foam, *Proc. Inst. Mech. Eng. C* 216 (12) (2002) 1153–1156.
- [10] W. Yang, et al., Review on auxetic materials, *J. Mater. Sci.* 39 (2004) 3269–3279.
- [11] A. Spadoni, M. Ruzzene, S. Gonella, F. Scarpa, Phononic properties of hexagonal chiral lattices, *Wave Motion* 46 (7) (2009) 435–450.
- [12] A. Alderson, K.L. Alderson, D. Attard, K.E. Evans, R. Gatt, J.N. Grima, W. Miller, N. Ravirala, C.W. Smith, K. Zied, Elastic constants of 3-, 4- and 6-connected chiral and anti-chiral honeycombs subject to uniaxial in-plane loading, *Compos. Sci. Technol.* 70 (7) (2010) 1042–1048.
- [13] J. Dirrenberger, S. Forest, D. Jeulin, C. Colin, Homogenization of periodic auxetic materials, in: 11th International Conference on the Mechanical Behavior of Materials (ICM11), *Procedia Eng.* 10 (2011) 1847–1852, <http://dx.doi.org/10.1016/j.proeng.2011.04.307>.
- [14] E. Pasternak, A. Dyskin, Materials and structures with macroscopic negative Poisson's ratio, *Internat. J. Engrg. Sci.* 52 (2012) 103–114.
- [15] J.C. Alvarez Elipe, A. Diaz Lantada, Comparative study of auxetic geometries by means of computer-aided design and engineering, *Smart Mater. Struct.* 21 (2012) 105004.
- [16] J. Dirrenberger, S. Forest, D. Jeulin, Elastoplasticity of auxetic materials, *Comput. Mater. Sci.* 64 (2012) 57–61, <http://dx.doi.org/10.1016/j.commatsci.2012.03.036>.
- [17] J. Dirrenberger, S. Forest, D. Jeulin, Effective elastic properties of auxetic microstructures: anisotropy and structural applications, *Int. J. Mech. Mater. Des.* 9 (1) (2013) 21–33, <http://dx.doi.org/10.1007/s10999-012-9192-8>.
- [18] N. Kaminakis, G. Drosopoulos, G. Stavroulakis, Design and verification of auxetic microstructures using topology optimization and homogenization, *Arch. Appl. Mech.* 85 (9) (2015) 1289–1306.
- [19] C. Körner, Y. Liebold-Ribeiro, A systematic approach to identify cellular auxetic materials, *Smart Mater. Struct.* 24 (2) (2015) 025013.
- [20] K.K. Saxena, R. Das, E.P. Calius, Three decades of auxetics research– materials with negative Poisson's ratio: a review, *Adv. Energy Mater.* 18 (11) (2016) 1847–1870.
- [21] Z.P. Wang, L.H. Poh, J. Dirrenberger, Y. Zhu, S. Forest, Isogeometric shape optimization of smoothed petal auxetic structures via computational periodic homogenization, *Comput. Methods Appl. Mech. Engrg.* 323 (2017) 250–271.
- [22] N. Karathanasopoulos, H. Reda, J. Ganghoffer, Designing two-dimensional metamaterials of controlled static and dynamic properties, *Comput. Mater. Sci.* 138 (2017) 323–332.
- [23] N. Karathanasopoulos, F. Dos Reis, H. Reda, J. Ganghoffer, Computing the effective bulk and normal to shear properties of common two-dimensional architected materials, *Comput. Mater. Sci.* 154 (2018) 284–294.
- [24] Z.-P. Wang, L.H. Poh, Y. Zhu, J. Dirrenberger, S. Forest, Systematic design of tetra-petals auxetic structures with stiffness constraint, *Mater. Des.* 170 (2019) 107669.
- [25] C.T. Herakovich, Composite laminates with negative through-the-thickness Poisson's ratios, *J. Compos. Mater.* 18 (5) (1984) 447–455.
- [26] R.F. Almgren, An isotropic three-dimensional structure with Poisson's ratio=-1, *J. Elasticity* 15 (1985) 427–430.
- [27] R.J. Bathurst, L. Rothenburg, Note on a random isotropic granular material with negative Poisson's ratio, *Internat. J. Engrg. Sci.* 26 (4) (1988) 373–383.
- [28] B.D. Caddock, K.E. Evans, Microporous materials with negative Poisson's ratios: I. Microstructure and mechanical properties, *J. Phys. D: Appl. Phys.* 22 (1989) 1877–1882.
- [29] T.P. Hughes, A. Marmier, K.E. Evans, Auxetic frameworks inspired by cubic crystals, *Int. J. Solids Struct.* 47 (2010) 1469–1476.
- [30] A.W. Lipsett, A.I. Beltzer, Reexamination of dynamic problems of elasticity for negative Poisson's ratio, *J. Acoust. Soc. Am.* 84 (6) (1988) 2179–2186.
- [31] N. Chan, K.E. Evans, Indentation resilience of conventional and auxetic foams, *J. Cell. Plast.* 34 (3) (1998) 231–260, <http://dx.doi.org/10.1177/0021955X9803400304>.
- [32] J.B. Choi, R.S. Lakes, Fracture toughness of re-entrant foam materials with a negative Poisson's ratio: experiment and analysis, *Int. J. Fract.* 80 (1996) 73–83.
- [33] G. Rosi, N. Auffray, Anisotropic and dispersive wave propagation within strain-gradient framework, *Wave Motion* 63 (2016) 120–134.
- [34] W. Liu, N. Wang, T. Luo, Z. Lin, In-plane dynamic crushing of re-entrant auxetic cellular structure, *Mater. Des.* 100 (2016) 84–91, <http://dx.doi.org/10.1016/j.matdes.2016.03.086>, URL <http://www.sciencedirect.com/science/article/pii/S0264127516303707>.
- [35] T. Li, Y. Chen, X. Hu, Y. Li, L. Wang, Exploiting negative Poisson's ratio to design 3d-printed composites with enhanced mechanical properties, *Mater. Des.* 142 (2018) 247–258, <http://dx.doi.org/10.1016/j.matdes.2018.01.034>, URL <http://www.sciencedirect.com/science/article/pii/S026412751830042X>.
- [36] N. Novak, L. Starčević, M. Vesenjāk, Z. Ren, Blast response study of the sandwich composite panels with 3d chiral auxetic core, *Compos. Struct.* 210 (2019) 167–178, <http://dx.doi.org/10.1016/j.compstruct.2018.11.050>, URL <http://www.sciencedirect.com/science/article/pii/S0263822318336845>.
- [37] H.C. Kim, D.K. Shin, J.J. Lee, J.B. Kwon, Crashworthiness of aluminum/cfrp square hollow section beam under axial impact loading for crash box application, *Compos. Struct.* 112 (2014) 1–10.
- [38] I. Maskery, N.T. Aboulkhair, A. Aremu, C. Tuck, I. Ashcroft, Compressive failure modes and energy absorption in additively manufactured double gyroid lattices, *Addit. Manuf.* 16 (2017) 24–29.
- [39] G.M. Luz, J.F. Mano, Biomimetic design of materials and biomaterials inspired by the structure of nacre, *Philos. Trans. R. Soc. Lond. Ser. A Math. Phys. Eng. Sci.* 367 (1893) (2009) 1587–1605.
- [40] U.G. Wegst, H. Bai, E. Saiz, A.P. Tomsia, R.O. Ritchie, Bioinspired structural materials, *Nature Mater.* 14 (1) (2015) 23.
- [41] Z. Yin, A. Dastjerdi, F. Barthelat, Tough and deformable glasses with bioinspired cross-ply architectures, *Acta Biomater.* 75 (2018) 439–450.

- [42] Z. Yin, F. Hannard, F. Barthelat, Impact-resistant nacre-like transparent materials, *Science* 364 (6447) (2019) 1260–1263.
- [43] S. Krauss, E. Monsonego-Orsan, E. Zelzer, P. Fratzl, R. Shahar, Mechanical function of a complex three-dimensional suture joining the bony elements in the shell of the red-ear slider turtle, *Adv. Mater.* 21 (2009) 407–412.
- [44] J. Dunlop, R. Weinkamer, P. Fratzl, Artful interfaces within biological materials, *Materials Today* 14 (3) (2011) 70–78.
- [45] D.W. Schaefer, J. Zhao, H. Dowty, M. Alexander, E.B. Orler, Carbon nanofibre reinforcement of soft materials, *Soft Matter* 4 (10) (2008) 2071, <http://dx.doi.org/10.1039/b805314f>, URL <http://xlink.rsc.org/?DOI=b805314f>.
- [46] J. Dirrenberger, S. Forest, D. Jeulin, Towards gigantic RVE sizes for stochastic fibrous networks, *Int. J. Solids Struct.* 51 (2) (2014) 359–376, <http://dx.doi.org/10.1016/j.ijsolstr.2013.10.011>.
- [47] S. Bapari, A.H. Chokshi, The role of the soft phase in rigidity enhancement in a particulate composite, *Composites A* 123 (2019) 114–122, <http://dx.doi.org/10.1016/j.compositesa.2019.04.004>, URL <http://www.sciencedirect.com/science/article/pii/S1359835X19301290>.
- [48] Y.W. Kwon, R.E. Cooke, C. Park, Representative unit-cell models for open-cell metal foams with or without elastic filler, *Mater. Sci. Eng. A* 343 (1) (2003) 63–70, [http://dx.doi.org/10.1016/S0921-5093\(02\)00360-X](http://dx.doi.org/10.1016/S0921-5093(02)00360-X), URL <http://www.sciencedirect.com/science/article/pii/S092150930200360X>.
- [49] S. Liu, A. Li, P. Xuan, Mechanical behavior of aluminum foam/polyurethane interpenetrating phase composites under monotonic and cyclic compression, *Composites A* 116 (2019) 87–97, <http://dx.doi.org/10.1016/j.compositesa.2018.10.026>, URL <http://www.sciencedirect.com/science/article/pii/S1359835X18304238>.
- [50] O. Al-Ketan, R.K.A. Al-Rub, R. Rowshan, Mechanical properties of a new type of architected interpenetrating phase composite materials, *Adv. Mater. Technol.* 2 (2) (2017) <http://dx.doi.org/10.1002/admt.201600235>, URL <http://onlinelibrary.wiley.com/doi/10.1002/admt.201600235/abstract>.
- [51] O. Al-Ketan, M. Adel Assad, R.K. Abu Al-Rub, Mechanical properties of periodic interpenetrating phase composites with novel architected microstructures, *Compos. Struct.* 176 (Supplement C) (2017) 9–19, <http://dx.doi.org/10.1016/j.compstruct.2017.05.026>, URL <http://www.sciencedirect.com/science/article/pii/S0263822316323157>.
- [52] G.J. Murray, F. Gandhi, Auxetic honeycombs with lossy polymeric infills for high damping structural materials, *J. Intell. Mater. Syst. Struct.* 24 (9) (2013) 1090–1104, <http://dx.doi.org/10.1177/1045389X13480569>, URL <http://journals.sagepub.com/doi/10.1177/1045389X13480569>.
- [53] T. Fila, P. Zlámal, O. Jiroušek, J. Falta, P. Koudelka, D. Kytýř, T. Doktor, J. Valach, Impact testing of polymer-filled auxetics using split hopkinson pressure bar, *Adv. Energy Mater.* 19 (10) (2017) <http://dx.doi.org/10.1002/adem.201700076>, URL <http://onlinelibrary.wiley.com/doi/10.1002/adem.201700076/abstract>.
- [54] J. Bernal Ostos, R.G. Rinaldi, C. m Hammetter, G.D. Stucky, F.W. Zok, A.J. Jacobsen, Deformation stabilization of lattice structures via foam addition, *Acta Mater.* 60 (19) (2012) 6476–6485, <http://dx.doi.org/10.1016/j.actamat.2012.07.053>, URL <http://www.sciencedirect.com/science/article/pii/S1359645412005010>.
- [55] N. Novak, L. Krstulović-Opara, Z. Ren, M. Vesenjak, Mechanical properties of hybrid metamaterial with auxetic chiral cellular structure and silicon filler, *Compos. Struct.* (2019) 111718, <http://dx.doi.org/10.1016/j.compstruct.2019.111718>, URL <https://linkinghub.elsevier.com/retrieve/pii/S0263822319323827>.
- [56] Y. Xue, W. Wang, F. Han, Enhanced compressive mechanical properties of aluminum based auxetic lattice structures filled with polymers, *Composites B* 171 (2019) 183–191, <http://dx.doi.org/10.1016/j.compositesb.2019.05.002>, URL <http://www.sciencedirect.com/science/article/pii/S1359836818335054>.
- [57] T. Strek, H. Jopek, E. Idczak, Computational design of two-phase auxetic structures, *Phys. Status Solidi (B)* 253 (7) (2016) 1387–1394.
- [58] H. Jopek, Finite element analysis of tunable composite tubes reinforced with auxetic structures, *Materials* 10 (12) (2017) 1359.
- [59] H. Jopek, T. Stręk, Thermoauxetic behavior of composite structures, *Materials* 11 (2) (2018) 294.
- [60] X.-L. Peng, C. Soyarslan, S. Bargmann, Phase contrast mediated switch of auxetic mechanism in composites of infilled re-entrant honeycomb microstructures, *Extrem. Mech. Lett.* 35 (2020) 100641, <http://dx.doi.org/10.1016/j.eml.2020.100641>, URL <https://linkinghub.elsevier.com/retrieve/pii/S235243162030016X>.
- [61] Z. Zhang, H. Zhu, R. Yuan, S. Wang, T. Fan, Y. Rezgui, D. Zhang, Auxetic interpenetrating composites: A new approach to non-porous materials with a negative or zero Poisson's ratio, *Compos. Struct.* 243 (2020) 112195, <http://dx.doi.org/10.1016/j.compstruct.2020.112195>, URL <http://www.sciencedirect.com/science/article/pii/S026382231933853X>.
- [62] X. Li, Y. Hao Tan, P. Wang, X. Su, H. Jean Willy, T. Seng Heng, J. Ding, Metallic microlattice and epoxy interpenetrating phase composites: Experimental and simulation studies on superior mechanical properties and their mechanisms, *Composites A* (2020) 105934, <http://dx.doi.org/10.1016/j.compositesa.2020.105934>, URL <http://www.sciencedirect.com/science/article/pii/S1359835X20301731>.
- [63] F. Albertini, J. Dirrenberger, A. Molotnikov, C. Sollogoub, Computational investigation of the effective mechanical behavior for 3D pre-buckled auxetic lattices, *J. Appl. Mech.* 86 (11) (2019) 111003, <http://dx.doi.org/10.1115/1.4044542>, URL <https://asmcdigitalcollection.asme.org/appliedmechanics/article/doi/10.1115/1.4044542/958339/Computational-Investigation-of-the-Effective>.
- [64] F. Warmuth, M. Wormser, C. Körner, Single phase 3d phononic band gap material, *Sci. Rep.* 7 (1) (2017) 3843, <http://dx.doi.org/10.1038/s41598-017-04235-1>, URL <https://www.nature.com/articles/s41598-017-04235-1>.
- [65] F. Warmuth, F. Osmanlic, L. Adler, M.A. Lodes, C. Körner, Fabrication and characterisation of a fully auxetic 3d lattice structure via selective electron beam melting, *Smart Mater. Struct.* 26 (2) (2017) 025013, <http://dx.doi.org/10.1088/1361-665X/26/2/025013>, URL <http://stacks.iop.org/0964-1726/26/i=2/a=025013?key=crossref.a48f66bcc73d2dad6e0079de9fc50ee>.
- [66] C. Körner, Y. Liebold-Ribeiro, A systematic approach to identify cellular auxetic materials, *Smart Mater. Struct.* 24 (2) (2015) 025013.
- [67] Stratsys. [link]. URL <https://www.stratsys.com/en/3d-printers/objet-350-500-connex3>.
- [68] G. Loh, E. Pei, D. Harrison, M. Monzón, An overview of functionally graded additive manufacturing, *Addit. Manuf.* 23 (2018) 34–44.
- [69] Y. Tee, P. Tran, M. Leary, P. Pille, M. Brandt, 3d printing of polymer composites with material jetting: Mechanical and fractographic analysis, *Addit. Manuf.* 36 (2020) 101558.
- [70] L. Djumas, G.P. Simon, Y. Estrin, A. Molotnikov, Deformation mechanics of non-planar topologically interlocked assemblies with structural hierarchy and varying geometry, *Sci. Rep.* 7 (1) (2017) 11844.
- [71] A.-E. Viard, J. Dirrenberger, S. Forest, Propagating material instabilities in planar architected materials, *Int. J. Solids Struct.* 202 (2020) 532–551, <http://dx.doi.org/10.1016/j.ijsolstr.2020.05.027>, URL <http://www.sciencedirect.com/science/article/pii/S0020768320302006>.
- [72] E.M. Arruda, M.C. Boyce, A three-dimensional constitutive model for the large stretch behavior of rubber elastic materials, *J. Mech. Phys. Solids* 41 (2) (1993) 389–412, [http://dx.doi.org/10.1016/0022-5096\(93\)90013-6](http://dx.doi.org/10.1016/0022-5096(93)90013-6), URL <http://www.sciencedirect.com/science/article/pii/0022509693900136>.
- [73] C. Geuzaine, J.-F. Remacle, Gmsh: A 3-D finite element mesh generator with built-in pre- and post-processing facilities, *Internat. J. Numer. Methods Engrg.* 79 (11) (2009) 1309–1331, <http://dx.doi.org/10.1002/nme.2579>, URL <https://onlinelibrary.wiley.com/doi/abs/10.1002/nme.2579>.
- [74] D. Jeulin, Caractérisation Morphologique et Modèles de Structures Aléatoires, in: *Homogénéisation en Mécanique des Matériaux*, vol. 1, Hermès, 2001, pp. 95–132, (Ch. 4).
- [75] S. Torquato, *Random Heterogeneous Materials*, Springer, 2001.
- [76] M. Assidi, J.-F. Ganghoffer, Composites with auxetic inclusions showing both an auxetic behavior and enhancement of their mechanical properties, *Compos. Struct.* 94 (8) (2012) 2373–2382.
- [77] K. El Nady, F. Dos Reis, J. Ganghoffer, Computation of the homogenized nonlinear elastic response of 2d and 3d auxetic structures based on micropolar continuum models, *Compos. Struct.* 170 (2017) 271–290.
- [78] J. Dirrenberger, S. Forest, D. Jeulin, Computational homogenization of architected materials, in: Y. Estrin, Y. Bréchet, J. Dunlop, P. Fratzl (Eds.), *Architected Materials in Nature and Engineering*, in: Springer Series in Materials Science, vol. 282, Springer, 2019, pp. 89–139, [http://dx.doi.org/10.1007/978-3-030-11942-3\\_4](http://dx.doi.org/10.1007/978-3-030-11942-3_4), (Ch. 4).
- [79] H.J. Bunge, *Texture Analysis in Materials Science*, Butterworths, 1982.
- [80] M.M. Osman, M. Shazly, E.A. El-Danaf, P. Jamshidi, M.M. Attallah, Compressive behavior of stretched and composite microlattice metamaterial for energy absorption applications, *Composites B* 184 (2020) 107715, <http://dx.doi.org/10.1016/j.compositesb.2019.107715>, URL <http://www.sciencedirect.com/science/article/pii/S135983681932462X>.